ACS APPLIED NANO MATERIALS

www.acsanm.org Article

Selective Actuation and Tomographic Imaging of Swarming Magnetite Nanoparticles

Klaas Bente, Anna C. Bakenecker, Anselm von Gladiss, Felix Bachmann, Andrejs Cēbers, Thorsten M. Buzug, and Damien Faivre*

Cite This: *ACS Appl. Nano Mater.* 2021, 4, 6752−6759 Read Online

ACCESS | Metrics & More | Article Recommendations | Supporting Information

ABSTRACT: Micro- and nanomotors have seen substantial progress in recent years for biomedical applications. However, three grand challenges remain: (i) high velocities to overcome the blood flow, (ii) spatially selective control to enable complex navigation, and (iii) integration of a medical, tomographic real-time imaging method to acquire feedback information. Here, we report the combination of active magnetic matter and a medical imaging technique, namely magnetic particle imaging (MPI), which addresses these needs. We synthesize ∼200 nm magnetic nanoparticles and observe a macroscopic, collective effect in a homogeneous magnetic field with a rotating field vector. The nanoparticles form a millimeter-sized cloud and reach speeds of 8 mm s^{-1}. This cloud is imaged and selectively steered with an MPI scanner. Our experimental results are supported by a model that highlights the role of the Mason number, the particle's volume fraction, and the height of the cloud. The successful introduction of a fast swarm of microscopic units and the spatial selectivity of the technique suggest an effective approach to translate the use of micro- and nanobots into a clinical application.

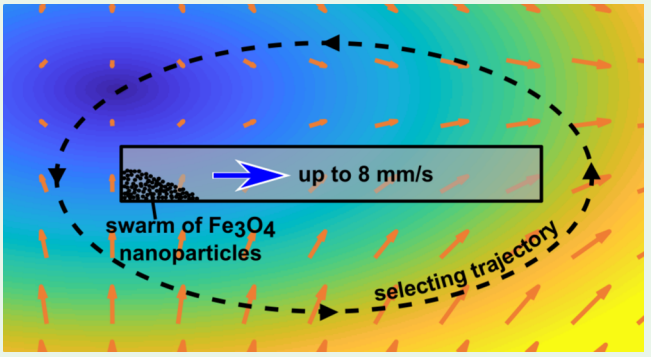

KEYWORDS: *collective effects, magnetic steering, nanobots, active matter, magnetic particle imaging, MPI, microrobotics, nanorobotics*

INTRODUCTION

In the emerging field of nano- and microrobotics, most applications aim toward untethered microscopic devices operating inside the human body.[1−4] The goal of such operations range from targeted drug delivery[5,6] to micro-surgery,[7] with most recent progress focusing toward bio-compatibility and degradability.[8] However, the size of the individual units, currently ranging from 1 to 200 μm, are likely to cause occlusions in small (3−10 μm) capillaries.[9] At the same time, movement speeds in the range of several mm s^{-1} are necessary to navigate against the blood flow of vascular systems (0.25−1.5 mm s^{-1}).[10] These demands work against each other for most of the magnetic microbot locomotion approaches investigated so far since these devices couple their geometrical shape to their movement speed, leading to a speed-size constraint.[11,12]

Another fundamental challenge is the medical imaging of such devices. While imaging is clearly mandatory for actively guided devices, feedback information for autonomously acting devices will be necessary to monitor their actions. Recently, first in vitro trials were performed for swarms of swimmers in a positron emission tomography scanner[13] and for individual swimmers using optical imaging with a millimeter-deep penetration depth.[14] However, these approaches either work with ionizing radiation, which is especially disadvantageous for long-term tracking of a moving device, or are severely limited in imaging penetration depth, making a full-body approach impossible to achieve. Additional approaches include fluorescent imaging, ultrasound imaging, computed tomography, magnetic resonance imaging, and single-photon computed tomography (summed up in refs 15 and 16). The advantage of these imaging techniques is that they are established in clinical routines. However, limitations in penetration depth, low temporal or spatial resolution, or the utilized ionizing radiation will constitute difficulties for a successful implementation in the clinic for each of those techniques. As an additional drawback, all of these approaches significantly increase the complexity of the whole procedure. Namely, the imaging units and the steering mechanisms are based on different physical concepts and therefore require multiple detectors, emitters, and control units in the vicinity of the samples. Magnetic particle imaging (MPI), however, is an emerging, tracer-based, tomographic, three-dimensional imaging technique, capable of

Received: March 22, 2021
Accepted: June 15, 2021
Published: July 12, 2021

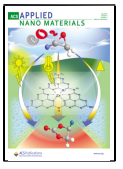

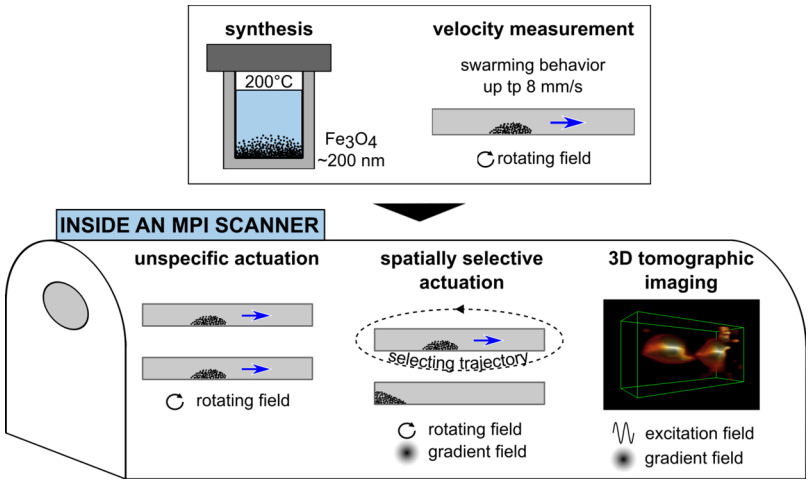

Figure 1. Nanoparticle cloud actuation and imaging. Magnetite nanoparticles with an average diameter of 200 nm were synthesized in a solvothermal reduction method. These particles showed a swarming behavior that led to high movement speeds of the resulting nanoparticle cloud in a homogeneous magnetic field with a rotating field vector. The magnetic fields of an MPI scanner were used to control multiples of these clouds simultaneously and spatially selectively. The same scanner was used to image the spatial distribution of the particles, achieving imaging and control in one device.

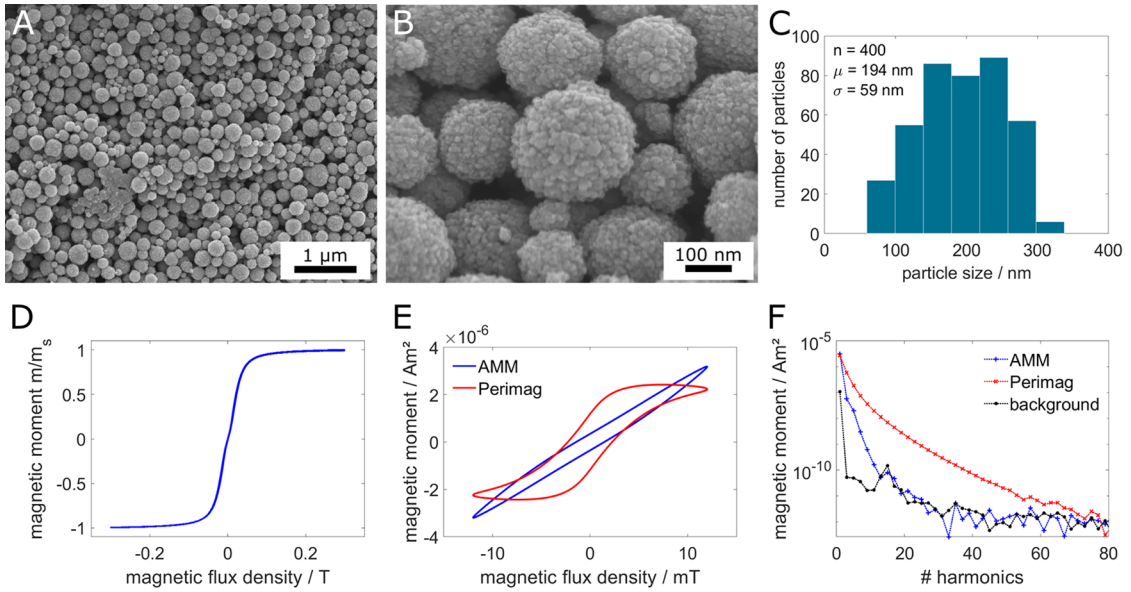

Figure 2. Properties of AMM. (A,B) SEM images of different magnifications. (C) Particle size distribution with a sample size of n = 400. (D) Magnetization behavior of AMM measured with a vibrating sample magnetometer. The magnetic moment m is normalized by the saturation magnetic moment m_s, which is reached at about 150 mT. (E) Magnetic particle spectrometer measurement shows the dynamic hysteresis at very similar parameters as in the MPI scanner (25 kHz, 12 mT) compared to a well suitable MPI tracer (Perimag, 30 μL, 1:10 dilution). (F) Amplitude spectrum shows the odd harmonics and a detectable signal up to the 11th harmonic.

visualizing the concentration distribution of superparamagnetic nanoparticles.[17] To date, MPI is a preclinical method. One of its strengths lies in vascular imaging as it is free of ionizing radiation and provides real-time visualization.[18,19] Recent studies demonstrated that the magnetic fields of MPI scanners can not only be used for imaging but also for steering magnetic devices of centimeter[20,21] and millimeter[22] size by rotating magnetic fields. However, control of microscopic devices and swarms as well as their spatial selective control has remained unexplored.

In general, spatial selective control of microbots is an open challenge for most investigated micro- and nanobot actuation techniques. Some advances were made for example by chemical or light-based activation of microswimmers.[23] However, feedback-based selective control has not been reported so far but is required for controlling several entities or swarms during application scenarios. Here, we propose a strategy based on MPI and magnetite nanoparticles that simultaneously addresses the three mentioned challenges: size-speed constraint, spatial selective control, and medical imaging. A high-speed collective rolling effect of nanometer-sized magnetite nanoparticles is achieved in a tubular structure by applying a rotating magnetic field with an MPI scanner. Spatial selectivity is obtained by using superimposed gradient fields. Finally, tomographic imaging is performed using MPI, which relies on the nonlinear magnetization behavior of the swarm's constituents.[17] Overall, we demonstrate how an MPI scanner is

https://doi.org/10.1021/acsanm.1c00768
ACS Appl. Nano Mater. 2021, 4, 6752−6759

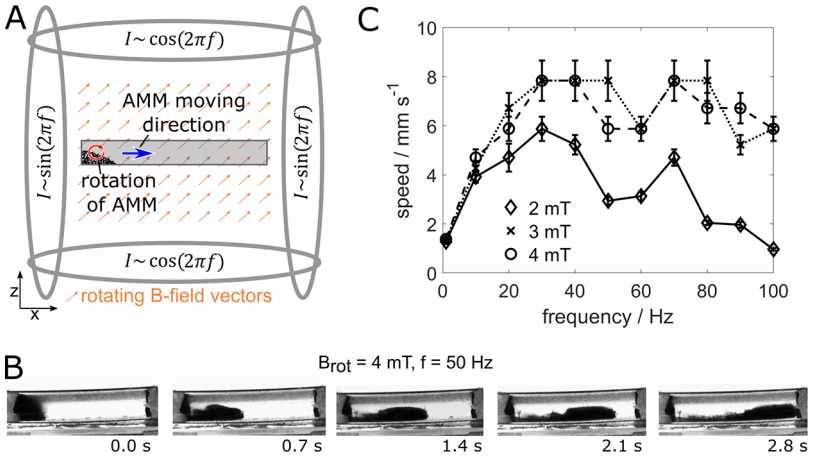

Figure 3. AMM forms a particle cloud in the presence of a rotating magnetic field showing high movement speeds. (A) Two pairs of Helmholtz coils generated a homogeneous magnetic field with a rotating magnetic field vector. The setup is capable of frequencies up to 100 Hz and field amplitudes up to 4 mT. The rotation happened in the x−z-plane. (B) Video stills of the actuation with a frequency of 50 Hz and an amplitude of 4 mT. (C) Cloud speeds for different frequencies (starting at 1 Hz) and field strengths. The error bars result from estimated time measurement errors. The maximum speeds were 8 mm s^{-1}. The experiments were conducted in a sealed polyvinyl alcohol tube (3 mm inner diameter and 26 mm long).

capable of propelling, selecting, and imaging swarms of nanoparticles (see Figure 1).

EXPERIMENTAL SECTION AND RESULTS

Active Magnetic Matter. Magnetite nanoparticles were produced with a solvothermal reduction method[24] (see Supporting Information). Scanning electron microscopy (SEM) images are shown in Figure 2a,b. The mean diameter of AMM particles was measured to be 194 nm with a standard deviation of 59 nm (distribution in Figure 2c) from such SEM images. A vibrating sample magnetometer was used to determine the magnetization behavior of the AMM (Figure 2d). The saturation magnetization of AMM is reached at a magnetic flux density of about 150 mT. The dynamic magnetization curve, which is magnetization dependent on the excitation field, was acquired with a magnetic particle spectrometer with one-dimensional excitation.[25,26] The magnetization curve shows a dynamic hysteresis and an almost linear magnetization behavior (see Figure 2e). The dynamic magnetization behavior is compared to the behavior of Perimag, a commercially available superparamagnetic iron oxide nanoparticle dispersion, which is optimized for and one current standard in MPI.[27] This sample shows a strong nonlinearity in its magnetization curve, which explains numerous harmonics in the amplitude spectrum (see Figure 2f). For AMM, harmonics up to the 11th are distinguishable from the background, indicating that MPI is feasible but with lower sensitivity and spatial resolution compared to Perimag.

We dispersed the nanoparticles in water at a molar iron concentration of 125 mM. The dispersion was then transferred into polyvinyl alcohol tubes for all following experiments. The particles sedimented and were collected and concentrated at one end of the tube with a permanent magnet. In the presence of a homogeneous and rotating magnetic field of a Helmholtz coil setup (see Figure 3a), the particles self-assembled to form a dynamic cloud, which moved inside the plane of rotation on the bottom surface of the tube, as depicted in Figure 3b (Movie S1). The shape of the cloud is a result of sedimentation, the shape of the tube, and magnetic interactions, as described in our theoretical model. This cloud was an out-of-equilibrium state of the assembly of magnetic nanoparticles, which we call AMM.[28] Remarkably, this AMM moved with a velocity of up to 8 mm s^{-1} at a rotating field frequency of 40 Hz (Figure 3c). For comparison with other micro- and nanobot approaches, the speed can also be described as 40,000 body length s^{-1} (body length meaning the diameter of a single particle) or as a dimensionless speed (body lengths per turn) of 1000 (calculated via $vf^{-1}d^{-1}$, where v is the velocity, f the frequency, and d the particle diameter). Due to the collective effect, the cloud travels more than 300 times faster than a single particle would. A theoretical model was developed and describes the two most crucial behaviors of the system: the high speed and the independence of speed from the magnetic field's rotation frequency after a critical frequency (see Figure 3c).

Calculation of Cloud Height. Attractive forces between the magnetic nanoparticles in a rotating field make the behavior of their suspension similar to the behavior of liquid droplets, such as oil in water. Its shape is due to the action of gravity and may be found using the methods of capillary hydrodynamics. Since the radius of the cloud is much larger than its thickness, it can be found by the solution of the 2D problem.

The pressure in the cloud (p_2) and around (p_1) is given by

$$p_2 = p_0 + \rho_2 g(h - z) \text{ and } p_1 = p_0 + \rho_1 g(h - z)$$

where ρ_2 is the density of the cloud, ρ_1 is the density of the surrounding liquid, h is the thickness of the cloud in the central region, and p_0 is the atmospheric pressure. Introducing the tangent angle of the cloud's interface $\vartheta(l)$ (l is the natural parameter), the condition of the capillary equilibrium reads

$$(\rho_2 - \rho_1)g(h - z) = \sigma \frac{\mathrm{d}\vartheta}{\mathrm{d}l}$$

with the surface tension $\sigma = \mu_0 M^2 a/24$ estimated as the magnetic interaction, where M is the magnetization, μ_0 is the vacuum permeability, and a is the particle radius. By differentiation and with $\frac{\mathrm{d}z}{\mathrm{d}l} = \sin\vartheta$, the equation

$$\frac{\mathrm{d}^2\vartheta}{\mathrm{d}l^2} + \frac{\Delta\rho g}{\sigma}\sin\vartheta = 0$$

follows. It is solved at boundary conditions $\vartheta(0) = 0$ (we assume complete nonwetting) and $\vartheta(\infty) = \pi$ (interface of the cloud). The solution reads

$$\vartheta(l) = 4\arctan\left(\tanh\left(\sqrt{\frac{\Delta\rho g}{4\sigma}}\, l\right)\right)$$

The shape of the cloud can be found by numerically integrating the set of equations

$$\frac{\mathrm{d}x}{\mathrm{d}l} = \cos\vartheta \text{ and } \frac{\mathrm{d}z}{\mathrm{d}l} = \sin\vartheta$$

https://doi.org/10.1021/acsanm.1c00768
ACS Appl. Nano Mater. 2021, 4, 6752−6759

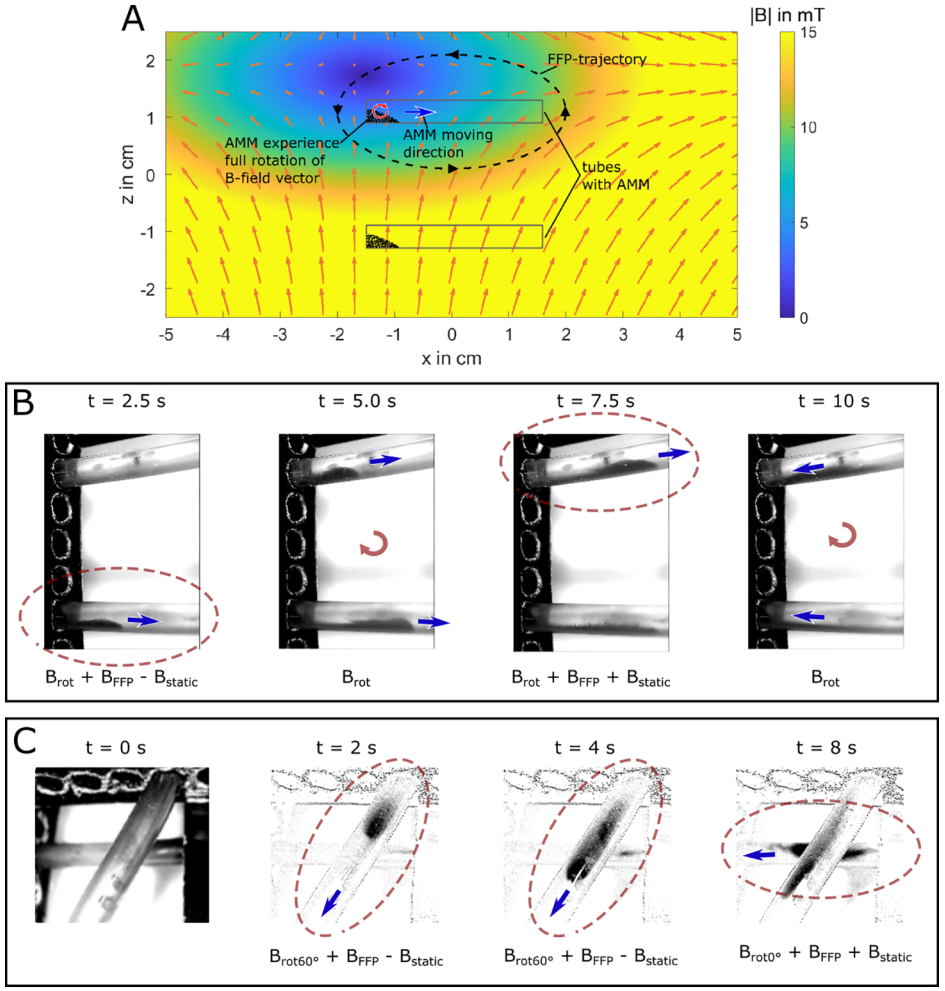

Figure 4. Selective control of AMM inside an MPI scanner. (A) Magnetic field configuration for selective actuation. A gradient field B_{FFP} of 0.6 T m^{-1} in z (0.3 T m^{-1} in x and y) and a static field B_{static} of ±6.6 mT to select the AMM inside the upper or the lower tube, respectively. The tubes have a distance of 22 mm to each other. A rotating magnetic field B_{rot} is superimposed with the rotation plane in x/z with an amplitude of 6 mT, generating an ellipsoidal trajectory of the FFP. Only within the ellipsoid, the field vector is fully rotating. Note that the FFP moves in the opposite direction to that of the field vector. (B) Side view of a selective control experiment with two parallel aligned tubes. A rotation frequency of 10 Hz was applied; field and gradient strengths were the same as shown in (A). It was possible to steer the AMM in the bottom tube, then both AMMs simultaneously, then only the AMM in the top tube, and then both AMMs backward. (C) Bottom view on a two-tube-experiment where one tube was positioned at an angle of 60° to the other. The distance was 24 mm. A static field of ±7.2 mT was applied. The plane of rotation of B_{rot} had to be adapted accordingly. For better visibility of the moving AMM, subtraction images are shown. The first image was subtracted from the subsequent frames. Blue arrows indicate the AMM movement direction. Dashed lines indicate the trajectory of the FFP. The animated field configuration and the corresponding videos can be found in Supporting Information.

The cloud has a finite thickness in the applied rotating field. This can be represented as surface tension which may be estimated as originating from magnetic interactions. The equilibrium thickness of the cloud coming from the balance of capillary and gravity forces in the 2D case may be estimated as $z(\infty) = h = \sqrt{\frac{4\sigma}{\Delta\rho g}}$.[29] The concentration and density of magnetite in water give $\Delta\rho$ = 1.35 g/cm^3. From the surface tension estimation follows σ = 1.2 mJ/m^2, when considering the saturation magnetization M = 480 kA/m of magnetite and a = 100 nm. With these values, a cloud thickness of $h \approx$ 0.6 mm results. This is in the same order of magnitude as in the observations, where roughly half the tube radius is occupied (resulting in $h \approx$ 1.5 mm). We should mention that our calculated value may be overestimated since the particles are polydomain and their remanent magnetization is smaller than the saturation magnetization. Nevertheless, it allows rationalizing the observations according to which the thickness of the cloud is larger with the rotating magnetic field activated.

Calculation of Cloud Velocity. The behavior of the cloud in the rotating field is reduced to the problem of the flow of the cloud induced by the rotation of magnetic particles. This is a typical problem of flow caused by antisymmetric stress σ^a_{ik} acting on a free interface.[30] In our case, we have an infinite layer, the angular velocity of the field $\vec{\omega} = (-\omega, 0, 0)$, a synchronous rotation of the particles, and the field $\sigma^a_{ik} = \frac{1}{2}e_{ikl}K_l$, where $\vec{K} = (-\alpha\omega, 0, 0)$ (α is the coefficient of the rotational drag per unit volume).

The condition for the absence of tangential stress on the free interface

$$\left(\eta \frac{dv_y}{dz} - \frac{\alpha}{2}\omega\right)\Bigg|_{z=h} = 0$$

gives $v_y = \frac{\alpha}{2\eta}\omega z$ and for the velocity of the free interface $v_{int} = \frac{\alpha}{2\eta}\omega h$, with η being the viscosity of the cloud. The mean velocity which we may identify as the velocity of the cloud is

https://doi.org/10.1021/acsanm.1c00768
ACS Appl. Nano Mater. 2021, 4, 6752−6759

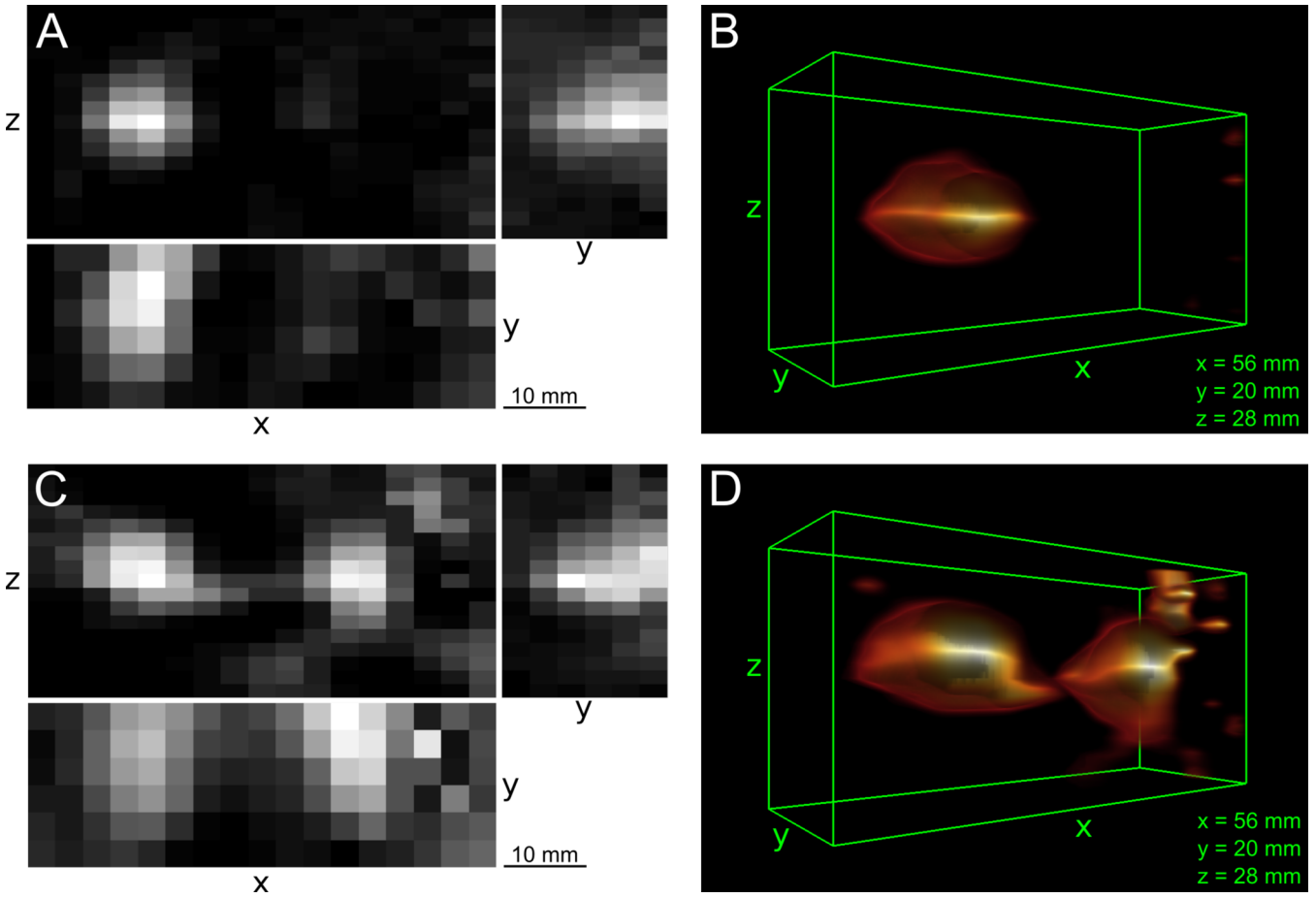

Figure 5. 3D localization of AMM using MPI before and after actuation. (A) Sagittal (*XZ*), coronal (*XY*), and axial (*YZ*) planes before actuation as well as (B) volume representation with an additional Gauss filtering. (C,D) show the equivalent images after actuation. The signal is visualized by normalized intensity values (range 0−1). A 360° view of the volume representations can be found in Supporting Information. A fraction of the nanoparticles did not move as it was stuck to the petroleum jelly that sealed the tube. The movement has been achieved using rotating fields of the same scanner with 10 Hz and 6 mT.

$$v_{\text{cloud}} = \frac{\alpha}{4\eta}\omega h$$

Next, the rotational drag coefficient $\alpha = n\alpha_0$ (n is the number of particles per unit volume) must be estimated. In the limit of elongated chainlike structures formed under the action of a rotating field, α_0 may be estimated as $\alpha_0 = 2\eta V(L/2a)^2$, where V is the particle volume, L is the chain length, and $2a$ is the particle diameter, hence $L/2a$ is the number of particles in the chain. In ref 31, it is shown that the number of particles in the chain is established such that the chain stays in the synchronous regime. An increase in the frequency of the rotating field causes the viscous forces to break the chain after a certain critical frequency. Numerical and physical experiments[31] showed that the number of particles in the chain to keep the synchronous regime can be estimated according to $\frac{L}{2a} = \frac{1}{\sqrt{Ma}}$ where

$$Ma = \frac{144\eta\omega}{\mu_0 M^2}$$

is the Mason number. In this regime, the velocity of the cloud v_{cloud} does not depend on the frequency of the field, which agrees with the experimental observation shown in Figure 3c. The critical Mason number Ma_c at the transition between the regimes where the velocity of the cloud increases with frequency and becomes constant may be estimated according to the experimental data from ref 32 to be $Ma_c \approx 0.1$. The critical frequency can be obtained from the experimental data shown in Figure 3c and is about 30 Hz. Using the viscosity of water (1 mPa·s), we can calculate the magnetization to be 14.7 kA/m, which is about 3% of the saturation magnetization of 480 kA/m of magnetite. This is a reasonable value for a rotating field with 4 mT amplitude as shown in the magnetization curve in Figure 2d, where about 7% is reached.

The velocity of the cloud at the transition to the chain-breaking regime for the suspension with the volume fraction of the particles $\varphi = nV = 0.07$ (calculated from the particle concentration with an estimated cloud volume) can be calculated using

$$v_{\text{cloud}} = \frac{\pi\varphi f_c h}{Ma_c}$$

resulting in velocities in the order of cm/s. This qualitatively agrees with the observed velocity of 0.8 cm/s.

The model makes the independence of the collective locomotion speed from the actuation frequency after a critical frequency intuitive: The particles form rotating chains under the influence of the external magnetic field. Higher frequencies lead to a higher rotation speed of these chains but also to shorter chain lengths. The model predicts the key ingredients of the observed high speeds as the Mason number, the particle's volume fraction, and the height of the cloud. The first and last parameters are influenced by the particle's magnetization, making it the core parameter of the technique.

Spatially Selective Control of AMM. The spatially selective control of the AMM was performed inside a preclinical MPI scanner with a method previously proposed for centimeter-sized screws[20] (see the Supporting Information for details). The used MPI scanner (MPI System 25/20 FF, Bruker BioSpin GmbH, Ettlingen, Germany) features three kinds of magnetic fields. The gradient field generates a

https://doi.org/10.1021/acsanm.1c00768
ACS Appl. Nano Mater. 2021, 4, 6752−6759

field-free point (FFP) and spatially encodes the particle signal. The drive field is a three-dimensional homogeneous field and excites the particles for imaging purposes. Frequencies around 25 kHz are used. Third, focus fields, which are homogeneous offset fields, are used to shift the field of view in space. To selectively steer AMM, sinusoidal currents (10Hz) with different phases were applied to the focus field coils, which generated a homogeneous rotating magnetic field inside the scanner. By superimposing the rotating field with the gradient field of the scanner, a FFP that traveled on an ellipsoidal trajectory was created. A more detailed description of how the magnetic fields of an MPI scanner can be used for actuation and of the applied field configuration can be found in Supporting Information. When the FFP was driven around a tube of choice, with the rotation axis perpendicular to the tube, only the AMM inside this tube experienced a fully rotating magnetic field vector, leading to a forward movement. Nanoparticles outside the FFP trajectory only experienced an oscillating magnetic field with directions never fully rotating. Hence, no net movement was induced in those tubes (a schematic drawing can be found in Figure 4a and in Movie S2).

An actuation sequence was applied to a phantom with two tubes as follows: Actuation of AMM in the bottom tube—actuation of AMM in both tubes (no gradient field)—actuation of AMM in the top tube—actuation of AMM in both tubes in the backward direction (changing the rotation direction of the rotating field vector). Video frames shortly before and at the end of each sequence are shown in Figure 4b. The video can be found in Supporting Information (Movie S3).

Further experiments were performed with more complex movements. Figure 4c shows video frames of the selective actuation in nonparallel tubes. The associated video can be found in Supporting Information (Movie S4). For such actuation in arbitrary directions, the plane of rotation of the field vector needs to be adapted to the intended direction of movement (full description can be found in the Supporting Information).

The videos and video frames from Figure 4 prove that individual swarms were selectively steered. The selection occurred as intended by the actuation sequences, described above.

Imaging AMM with MPI. The final goal is to ensure that the AMM can indeed be imaged using MPI. The magnetic properties indicate a positive answer, but the practical proof is shown below. A single tube was positioned inside the scanner, and a homogeneous rotating field (10 Hz and 6 mT, no spatially selective control) was applied. Figure 5 shows the sagittal, coronal, and axial plane of the reconstructed images as well as a volume representation before and after an actuation experiment (3D views in Movies S5 and S6). Details about the imaging parameters and the image reconstruction can be found in Supporting Information.

DISCUSSION AND CONCLUSIONS

While the behavior of micro- and nanobot swarms (with a relatively low number of individual units) on surfaces is becoming better understood,[33−36] centimeter-scale locomotion strategies with nanometer-scale constituents have not been investigated so far, such that the swarming behavior of magnetic particles became of great interest.[37,38] Rather than the development of a specific microbot, we propose a new kind of large-scale locomotion strategy that inherently allows for spatially selective control and imaging of a microbot swarm in a tubular structure by MPI. Additionally, our presented model highlights some critical parameters of the system, such as the Mason number, the volume fraction of particles, and the height of the cloud.

While the locomotion strategy proposed here is limited to a 2D surface, it is likely that AMM can also be formed using magnetic micro-propellers, similarly to a previous study where different models of locomotion could be achieved with a single swarming material.[39] Such propellers can then swim against gravity and move rapidly over surfaces. The biocompatibility of AMM must be investigated carefully in future studies. No coating has been used in our studies, which is often a fundamental constituent of established drug agents.[40] The biodegradation is likely to happen in the liver and spleen as has been reported for magnetite nanoparticles.[41]

MPI is an imaging technique under preclinical investigation, although first attempts toward clinical scanners have been made.[42] The visualization with MPI is especially advantageous since the scanner can not only be used for imaging the distribution of AMM but also for selective steering. Although AMM is visible in MPI, the image quality is reduced compared to the typically used tracer materials. However, the images show that live tracking of AMM is possible when imaging and actuation sequences are alternated faster.

Application scenarios of our technique include the formation and control of AMM with different kinds of therapeutic drugs. As an example, an AMM effect could be achieved with biodegradable magnetic microspheres (polymeric spheres, including magnetic nanoparticles and a drug). These can be actively guided to a target location and then thermally activated using hyperthermia to increase the drug and nanoparticle release. This process can again be monitored using the difference in the MPI signal of incorporated and free magnetic nanoparticles.[43,44] Also possible is the application in the inner ear for targeted drug delivery.[45] Another application scenario includes the guidance of AMM into vessel branches with occlusions. Such branches hardly take up passively transported drugs due to the hydrodynamics of such a system.[46,47]

The limit of the spatial selectivity of actuation is the magnetic field gradient. A higher gradient introduces relevant dragging forces onto the nanoparticles, tearing them away from surfaces and impeding the locomotion process. This could, however, be utilized to keep certain particles in the desired position. The gradient proposed here of 0.6 T m^{-1} constitutes a compromise between spatial selectivity and interference of the AMM formation process on the ground of the tubes. In future studies, the size and shape of the nanoparticles will be tuned to allow for larger gradients to achieve more precise spatial control and better imaging results. Furthermore, for the steering of AMM in longer tubes, the FFP trajectory needs to be adapted such that the center of the ellipsoid is moved with the speed of AMM. As already shown here, it is possible to change the plane of rotation such that the AMM can be steered around the corners or into vessel branches of choice.

In summary, we propose a new kind of high-speed propulsion mechanism of magnetic nanoparticles for biomedical applications. This study creates a new direction in active magnetic matter research, which includes the investigation physics of the system, leading to the observed high movement speeds on the one hand and research on biomedical applications on the other hand.

ASSOCIATED CONTENT

Supporting Information

The Supporting Information is available free of charge at https://pubs.acs.org/doi/10.1021/acsanm.1c00768.

Production of magnetic nanoparticles; size and magnetic properties of AMM particles; single-tube experiments for speed measurement; magnetic fields of an MPI scanner for selective control; schematic drawing of the magnetic

https://doi.org/10.1021/acsanm.1c00768
ACS Appl. Nano Mater. 2021, 4, 6752−6759

field orientation; spatially selective control of AMM; and imaging AMM with MPI (PDF)
Plane of rotation of B_{rot} (PDF)
Frequency-dependent velocity of AMM (MP4)
Animation of magnetic field configuration of an MPI scanner for selective control (MP4)
Selective control of AMM in parallel tubes inside MPI scanner (MP4)
Selective control of AMM in crossing tubes inside MPI scanner (MP4)
Animated 3D volume rendering of AMM with MPI before actuation (MP4)
Animated 3D volume rendering of AMM with MPI after actuation (MP4)

AUTHOR INFORMATION

Corresponding Author

Damien Faivre − *Department of Biomaterials, Max Planck Institute of Colloids and Interfaces, 14476 Potsdam, Germany; Aix-Marseille Université, CEA, CNRS, BIAM, F-13108 Saint-Paul-lez-Durance, France;* orcid.org/0000-0001-6191-3389; Email: damien.faivre@mpikg.mpg.de

Authors

Klaas Bente − *Department of Biomaterials, Max Planck Institute of Colloids and Interfaces, 14476 Potsdam, Germany;* orcid.org/0000-0002-2520-4697

Anna C. Bakenecker − *Institute of Medical Engineering, University of Lübeck, 23562 Lübeck, Germany; Fraunhofer Research Institution for Individualized and Cell-Based Medical Engineering IMTE, 23562 Lübeck, Germany;* orcid.org/0000-0002-9708-3476

Anselm von Gladiss − *Institute of Medical Engineering, University of Lübeck, 23562 Lübeck, Germany;* orcid.org/0000-0003-1340-4576

Felix Bachmann − *Department of Biomaterials, Max Planck Institute of Colloids and Interfaces, 14476 Potsdam, Germany;* orcid.org/0000-0002-7153-7441

Andrejs Cēbers − *MMML Lab, Department of Physics, University of Latvia, LV-1004 Riga, Latvia*

Thorsten M. Buzug − *Institute of Medical Engineering, University of Lübeck, 23562 Lübeck, Germany; Fraunhofer Research Institution for Individualized and Cell-Based Medical Engineering IMTE, 23562 Lübeck, Germany*

Complete contact information is available at: https://pubs.acs.org/10.1021/acsanm.1c00768

Author Contributions

K.B. and A.C.B. contributed equally to this work. K.B., A.C.B. and F.B. performed the experiments. A.v.G. realized the tomographic reconstruction. A.C. developed the model. K.B., A.C.B., and D.F. designed the experiments. D.F. and T.M.B. supervised the project. All authors contributed to writing the article.

Notes

The authors declare no competing financial interest.

ACKNOWLEDGMENTS

The authors gratefully acknowledge the support from the Max Planck Society and from the Federal Ministry of Education and Research, Germany (BMBF) for funding this project under grant no. 13GW0230B (FMT). A.C. is funded by the grant of Scientific Council of Latvia lzp-2020/1-0149. We thank Daniel Chevrier for discussions and proofreading.

REFERENCES

(1) Ghosh, A.; Fischer, P. Controlled Propulsion of Artificial Magnetic Nanostructured Propellers. *Nano Lett.* **2009**, *9*, 2243−2245.
(2) Dreyfus, R.; Baudry, J.; Roper, M. L.; Fermigier, M.; Stone, H. A.; Bibette, J. Microscopic artificial swimmers. *Nature* **2005**, *437*, 862−865.
(3) Bente, K.; Codutti, A.; Bachmann, F.; Faivre, D. Biohybrid and Bioinspired Magnetic Microswimmers. *Small* **2018**, *14*, 1704374.
(4) Sitti, M.; Ceylan, H.; Hu, W.; Giltinan, J.; Turan, M.; Yim, S.; Diller, E. Biomedical Applications of Untethered Mobile Milli/Microrobots. *Proc. IEEE* **2015**, *103*, 205−224.
(5) Felfoul, O.; Mohammadi, M.; Taherkhani, S.; de Lanauze, D.; Xu, Y. Z.; Loghin, D.; Essa, S.; Jancik, S.; Houle, D.; Lafleur, M.; Gaboury, L.; Tabrizian, M.; Kaou, N.; Atkin, M.; Vuong, T.; Batist, G.; Beauchemin, N.; Radzioch, D.; Martel, S. Magneto-aerotactic bacteria deliver drug-containing nanoliposomes to tumour hypoxic regions. *Nat. Nanotechnol.* **2016**, *11*, 941−947.
(6) Singh, A. V.; Sitti, M. Targeted Drug Delivery and Imaging Using Mobile Milli/Microrobots: A Promising Future Towards Theranostic Pharmaceutical Design. *Curr. Pharm. Des.* **2016**, *22*, 1418−1428.
(7) Srivastava, S. K.; Medina-Sánchez, M.; Koch, B.; Schmidt, O. G. Medibots: Dual-Action Biogenic Microdaggers for Single-Cell Surgery and Drug Release. *Adv. Mater.* **2016**, *28*, 832−837.
(8) Yan, X.; Zhou, Q.; Vincent, M.; Deng, Y.; Yu, J.; Xu, J.; Xu, T.; Tang, T.; Bian, L.; Wang, Y.-X. J.; Kostarelos, K.; Zhang, L. Multifunctional biohybrid magnetite microrobots for imaging-guided therapy. *Sci. Rob.* **2017**, *2*, No. eaaq1155.
(9) Arakawa, C.; Gunnarsson, C.; Howard, C.; Bernabeu, M.; Phong, K.; Yang, E.; DeForest, C. A.; Smith, J. D.; Zheng, Y. Biophysical and biomolecular interactions of malaria-infected erythrocytes in engineered human capillaries. *Sci. Adv.* **2020**, *6*, No. eaay7243.
(10) Hudetz, A. G. Blood Flow in the Cerebral Capillary Network: A Review Emphasizing Observations with Intravital Microscopy. *Microcirculation* **1997**, *4*, 233−252.
(11) Bachmann, F.; Bente, K.; Codutti, A.; Faivre, D. Using Shape Diversity on the Way to Structure-Function Designs for Magnetic Micropropellers. *Phys. Rev. Appl.* **2019**, *11*, 034039.
(12) Mirzae, Y.; Dubrovski, O.; Kenneth, O.; Morozov, K. I.; Leshansky, A. M. Geometric constraints and optimization in externally driven propulsion. *Sci. Rob.* **2018**, *3*, No. eaas8713.
(13) Vilela, D.; Cossío, U.; Parmar, J.; Martínez-Villacorta, A. M.; Gómez-Vallejo, V.; Llop, J.; Sánchez, S. Medical Imaging for the Tracking of Micromotors. *ACS Nano* **2018**, *12*, 1220−1227.
(14) Aziz, A.; Medina-Sánchez, M.; Claussen, J.; Schmidt, O. G. Real-Time Optoacoustic Tracking of Single Moving Micro-objects in Deep Phantom and Ex Vivo Tissues. *Nano Lett.* **2019**, *19*, 6612−6620.
(15) Pané, S.; Puigmartí-Luis, J.; Bergeles, C.; Chen, X.-Z.; Pellicer, E.; Sort, J.; Počepcová, V.; Ferreira, A.; Nelson, B. J. Imaging Technologies for Biomedical Micro- and Nanoswimmers. *Adv. Mater. Technol.* **2018**, *4*, 1800575.
(16) van Moolenbroek, G. T.; Patiño, T.; Llop, J.; Sánchez, S. Engineering Intelligent Nanosystems for Enhanced Medical Imaging. *Adv. Intell. Syst.* **2020**, *2*, 2000087.
(17) Gleich, B.; Weizenecker, J. Tomographic imaging using the nonlinear response of magnetic particles. *Nature* **2005**, *435*, 1214−1217.
(18) Weizenecker, J.; Gleich, B.; Rahmer, J.; Dahnke, H.; Borgert, J. "Three-dimensional real-timein vivomagnetic particle imaging. *Phys. Med. Biol.* **2009**, *54*, L1−L10.
(19) Bakenecker, A. C.; Ahlborg, M.; Debbeler, C.; Kaethner, C.; Buzug, T. M.; Lüdtke-Buzug, K. Magnetic particle imaging in vascular medicine. *Innov. Surg. Sci.* **2018**, *3*, 179−192.

(20) Rahmer, J.; Stehning, C.; Gleich, B. Spatially selective remote magnetic actuation of identical helical micromachines. *Sci. Rob.* **2017**, *2*, No. eaal2845.
(21) Bakenecker, A. C.; von Gladiss, A.; Friedrich, T.; Buzug, T. M. 3D-Printing with Incorporated Iron Particles for Magnetic Actuation and MPI. *Int. J. Mag. Part Imag.* **2020**, *6*, 003001.
(22) Bakenecker, A. C.; von Gladiss, A.; Friedrich, T.; Heinen, U.; Lehr, H.; Lüdtke-Buzug, K.; Buzug, T. M. Actuation and visualization of a magnetically coated swimmer with magnetic particle imaging. *J. Magn. Magn. Mater.* **2019**, *473*, 495−500.
(23) Dai, B.; Wang, J.; Xiong, Z.; Zhan, X.; Dai, W.; Li, C.-C.; Feng, S.-P.; Tang, J. Programmable artificial phototactic microswimmer. *Nat. Nanotechnol.* **2016**, *11*, 1087−1092.
(24) Deng, H.; Li, X.; Peng, Q.; Wang, X.; Chen, J.; Li, Y. Monodisperse Magnetic Single-Crystal Ferrite Microspheres. *Angew. Chem., Int. Ed.* **2005**, *44*, 2782−2785.
(25) Biederer, S.; Knopp, T.; Sattel, T. F.; Lüdtke-Buzug, K.; Gleich, B.; Weizenecker, J.; Borgert, J.; Buzug, T. M. Magnetization response spectroscopy of superparamagnetic nanoparticles for magnetic particle imaging. *J. Phys. D: Appl. Phys.* **2009**, *42*, 205007.
(26) Biederer, S.; Sattel, T. F.; Erbe, M.; Knopp, T.; Buzug, T. M. A Compensation Unit for a Magnetic Particle Spectrometer to Measure the Full Magnetization Spectrum of Superparamagnetic Iron Oxide Nanoparticles. *Biomed. Tech.* **2011**, *56*, 273.
(27) Eberbeck, D.; Dennis, C. L.; Huls, N. F.; Krycka, K. L.; Gruttner, C.; Westphal, F. Multicore Magnetic Nanoparticles for Magnetic Particle Imaging. *IEEE Trans. Magn.* **2013**, *49*, 269−274.
(28) Mandal, P.; Patil, G.; Kakoty, H.; Ghosh, A. Magnetic Active Matter Based on Helical Propulsion. *Acc. Chem. Res.* **2018**, *51*, 2689−2698.
(29) de Gennes, P. G. *Capillarity and Wetting Phenomena: Drops, Bubbles, Pearls, Waves*; Springer: New York, 2004.
(30) Tsebers, A. O. Internal rotation in the hydrodynamics of weakly conducting dielectric suspensions. *Fluid Dyn.* **1980**, *15*, 245−251.
(31) Melle, S.; Calderón, O. G.; Fuller, G. G.; Rubio, M. A. Polarizable Particle Aggregation Under Rotating Magnetic Fields Using Scattering Dichroism. *J. Colloid Interface Sci.* **2002**, *247*, 200−209.
(32) Melle, S.; Calderón, O. G.; Rubio, M. A.; Fuller, G. G. Microstructure evolution in magnetorheological suspensions governed by Mason number. *Phys. Rev. E* **2003**, *68*, 10.
(33) Xie, H.; Sun, M.; Fan, X.; Lin, Z.; Chen, W.; Wang, L.; Dong, L.; He, Q. Reconfigurable magnetic microrobot swarm: Multimode transformation, locomotion, and manipulation. *Sci. Rob.* **2019**, *4*, No. eaav8006.
(34) Yigit, B.; Alapan, Y.; Sitti, M. Programmable Collective Behavior in Dynamically Self-Assembled Mobile Microrobotic Swarms. *Adv. Sci.* **2019**, *6*, 1801837.
(35) Xie, H.; Fan, X.; Sun, M.; Lin, Z.; He, Q.; Sun, L. Programmable Generation and Motion Control of a Snakelike Magnetic Microrobot Swarm. *IEEE/ASME Trans. Mechatron.* **2019**, *24*, 902−912.
(36) Yu, J.; Wang, B.; Du, X.; Wang, Q.; Zhang, L. Ultra-extensible ribbon-like magnetic microswarm. *Nat. Commun.* **2018**, *9*, 3260.
(37) Wang, B.; Kostarelos, K.; Nelson, B. J.; Zhang, L. Trends in Micro-/Nanorobotics: Materials Development, Actuation, Localization, and System Integration for Biomedical Applications. *Adv. Mater.* **2020**, *33*, 2002047.
(38) Yu, J.; Yang, L.; Zhang, L. Pattern generation and motion control of a vortex-like paramagnetic nanoparticle swarm. *Int. J. Robot. Res.* **2018**, *37*, 912−930.
(39) Vach, P. J.; Faivre, D. The triathlon of magnetic actuation: Rolling, propelling, swimming with a single magnetic material. *Sci. Rep.* **2015**, *5*, 9364.
(40) Zhou, X. Y.; Tay, Z. W.; Chandrasekharan, P.; Yu, E. Y.; Hensley, D. W.; Orendorff, R.; Jeffris, K. E.; Mai, D.; Zheng, B.; Goodwill, P. W.; Conolly, S. M. Magnetic particle imaging for radiation-free, sensitive and high-contrast vascular imaging and cell tracking. *Curr. Opin. Chem. Biol.* **2018**, *45*, 131−138.
(41) Keselman, P.; Yu, E. Y.; Zhou, X. Y.; Goodwill, P. W.; Chandrasekharan, P.; Ferguson, R. M.; Khandhar, A. P.; Kemp, S. J.; Krishnan, K. M.; Zheng, B.; Conolly, S. M. Tracking short-term biodistribution and long-term clearance of SPIO tracers in magnetic particle imaging. *Phys Med. Biol.* **2017**, *62*, 3440−3453.
(42) Graeser, M.; Thieben, F.; Szwargulski, P.; Werner, F.; Gdaniec, N.; Boberg, M.; Griese, F.; Möddel, M.; Ludewig, P.; van de Ven, D.; Weber, O. M.; Woywode, O.; Gleich, B.; Knopp, T. Human-sized magnetic particle imaging for brain applications. *Nat. Commun.* **2019**, *10*, 1936.
(43) Zhu, X.; Li, J.; Peng, P.; Nassab, N. H.; Smith, B. R. Quantitative Drug Release Monitoring in Tumors of Living Subjects by Magnetic Particle Imaging Nanocomposite. *Nano Lett.* **2019**, *19*, 6725−6733.
(44) Zahn, D.; Weidner, A.; Nosrati, Z.; Wöckel, L.; Dellith, J.; Müller, R.; Saatchi, K.; Häfeli, U. O.; Dutz, S. Temperature controlled camptothecin release from biodegradable magnetic PLGA microspheres. *J. Magn. Magn. Mater.* **2019**, *469*, 698−703.
(45) Amokrane, W.; Belharet, K.; Souissi, M.; Grayeli, A. B.; Ferreira, A. Macro-micromanipulation platform for inner ear drug delivery. *Robo. Auton. Syst.* **2018**, *107*, 10−19.
(46) Griese, F.; Knopp, T.; Gruettner, C.; Thieben, F.; Müller, K.; Loges, S.; Ludewig, P.; Gdaniec, N. Simultaneous Magnetic Particle Imaging and Navigation of large superparamagnetic nanoparticles in bifurcation flow experiments. *J. Magn. Magn. Mater.* **2020**, *498*, 166206.
(47) Park, M.; Le, T.-A.; Eizad, A.; Yoon, J. A Novel Shared Guidance Scheme for Intelligent Haptic Interaction Based Swarm Control of Magnetic Nanoparticles in Blood Vessels. *IEEE Access* **2020**, *8*, 106714−106725.

https://doi.org/10.1021/acsanm.1c00768
ACS Appl. Nano Mater. 2021, 4, 6752−6759